

# Anisotropic Broadband Photoresponse of Layered Type-II Weyl Semimetal $\text{MoTe}_2$

Jiawei Lai, Xin Liu, Junchao Ma, Qinsheng Wang, Kenan Zhang, Xiao Ren, Yinan Liu, Qiangqiang Gu, Xiao Zhuo, Wei Lu, Yang Wu, Yuan Li, Ji Feng, Shuyun Zhou, Jian-Hao Chen,\* and Dong Sun\*

Photodetectors based on Weyl semimetal promise extreme performance in terms of highly sensitive, broadband and self-powered operation owing to its extraordinary material properties. Layered Type-II Weyl semimetal that break Lorentz invariance can be further integrated with other two-dimensional materials to form van der Waals heterostructures and realize multiple functionalities inheriting the advantages of other two-dimensional materials. Herein, we report the realization of a broadband self-powered photodetector based on Type-II Weyl semimetal  $\text{T}_d\text{-MoTe}_2$ . The prototype metal– $\text{MoTe}_2$ –metal photodetector exhibits a responsivity of  $0.40 \text{ mA W}^{-1}$  and specific directivity of  $1.07 \times 10^8$  Jones with  $43 \mu\text{s}$  response time at  $532 \text{ nm}$ . Broadband responses from  $532 \text{ nm}$  to  $10.6 \mu\text{m}$  are experimentally tested with a potential detection range extendable to far-infrared and terahertz. Furthermore, we identify the response of the detector is polarization angle sensitive due to the anisotropic response of  $\text{MoTe}_2$ . The anisotropy is found to be wavelength dependent, and the degree of anisotropy increases as the excitation wavelength gets closer to the Weyl nodes. In addition, with power and temperature dependent photoresponse measurements, the photocurrent generation mechanisms are investigated. Our results suggest this emerging class of materials can be harnessed for broadband angle sensitive, self-powered photodetection with decent responsivities.

applications.<sup>[1]</sup> Commercially available photodetectors are mainly based on semiconductors with the range of detection wavelength limited by their bandgap. In the visible and near-infrared region, the semiconductor-based photodetection technology is quite matured using classical materials such as silicon and InGaAs. However, in the mid-IR, photodetection without cooling using semiconducting materials remains a challenge.<sup>[2]</sup> Narrow bandgap semiconductors such as HgCdTe and PbSe, which are developed to detect the mid-infrared photons, generate a large dark current due to the thermal carriers at room temperature, limiting their operations mostly to the high-cost cryogenic temperature working under biased conditions.<sup>[3]</sup> The extreme case of narrowing down the gap of semiconductor ends up with a gapless semimetal. For a semimetal, the detection wavelength range is not limited by the bandgap. Although detectors based on semimetals cannot be operated with bias due to the lack of bandgap, the self-powered operations make them more suitable for portable and wearable appli-

cations. Over the past few years, a variety of photodetection devices based on semimetallic materials are explored. Graphene, the most widely studied semimetal for photodetection operations so far, was found to exhibit many advantages over traditional semiconductors, such as broadband detection from

Demand for the integratable and portable photosensing devices, especially those self-powered with room-temperature operation capability, attracts enormous research interest owing to their wide range of applications in imaging, remote sensing, environmental monitoring, optical communications, and analytical

J. Lai, X. Liu, J. Ma, Dr. Q. Wang, X. Ren, Y. Liu, Q. Gu, X. Zhuo, Dr. W. Lu, Prof. Y. Li, Prof. J. Feng, Prof. J.-H. Chen, Prof. D. Sun  
International Center for Quantum Materials  
School of Physics  
Peking University  
Beijing 100871, China  
E-mail: chenjianhao@pku.edu.cn; sundong@pku.edu.cn  
Dr. Q. Wang  
Beijing Key Laboratory of Nanophotonics and Ultrafine  
Optoelectronic Systems  
School of Physics  
Beijing Institute of Technology  
Beijing 100081, China

K. Zhang, Prof. S. Zhou  
State Key Laboratory of Low Dimensional Quantum Physics  
Department of Physics  
Tsinghua University  
Beijing 100084, China

Prof. Y. Wu  
Tsinghua-Foxconn Nanotechnology Research Center  
Tsinghua University  
Beijing 100084, China

Prof. Y. Li, Prof. J. Feng, Prof. S. Zhou, Prof. J.-H. Chen, Prof. D. Sun  
Collaborative Innovation Center of Quantum Matter  
Beijing 100871, China

DOI: 10.1002/adma.201707152

ultraviolet (UV) to terahertz (THz), lower dark current, ultrafast response time and tunable optical properties via electrostatic doping, and so on.<sup>[4]</sup> Most of these advantages, including broadband response, photothermoelectric (PTE) effect, and self-powered operation, are also exhibited by many other semimetallic materials such as 3D Dirac semimetal (DSM)  $\text{Cd}_3\text{As}_2$ ,<sup>[5]</sup> Weyl semimetal (WSM)  $\text{TaAs}$ ,<sup>[6]</sup> etc. Despite the lower photoresponsivity of semimetal-based photodetectors compared with the semiconductor-based ones in visible and near infrared wavelength region, novel properties in semimetals can boost the performance of photodetectors in other aspects such as mid-infrared wavelength operation, polarization sensitivity, flexible and wearable applications.

In this work, we investigate the performance of a field-effect photodetector device based on type-II WSM  $\text{T}_d$ - $\text{MoTe}_2$ . WSM is a topological semimetal in which bands disperse linearly in 3D momentum space.<sup>[7]</sup> Depending on the violation of Lorentz invariance, WSM is classified into two types: type-I,<sup>[8]</sup> where Weyl point is associated with a closed point-like Fermi surface, and type-II,<sup>[9]</sup> where Weyl point appears at the boundary of electron and hole pockets and exhibits very different transport properties from type-I WSM.  $\text{T}_d$ - $\text{MoTe}_2$ , which has an orthorhombic lattice structure breaking inversion symmetry, is an experimentally established type-II WSM.<sup>[9,10]</sup> Theoretical and experimental studies carried on WSMs so far mainly concern the band calculations, transport measurements of chiral anomaly, and angle-resolved photoemission spectroscopy measurements of topological related Fermi arcs.<sup>[10c-h,11]</sup> The photoresponse of WSMs, an essential factor toward new-generation photoelectric and electric devices, is largely unexplored. In terms of photodetection, WSM is expected to share several distinct advantages with DSMs, such as graphene and  $\text{Cd}_3\text{As}_2$ . These advantages include broadband PTE response as semimetallic materials and high responsibility as a result of linear dispersion and suppressed backscattering.<sup>[4b,5,12]</sup> Indeed, the carrier mobility is extremely high around the Weyl node, comparable or even exceeding that of graphene.<sup>[13]</sup> On the other hand, in contrast to graphene and similar to  $\text{Cd}_3\text{As}_2$ , the linear dispersion holds along all the three dimensions over certain energy range, which ensures the efficient carrier transport along all the directions. Besides the similarity with DSMs, WSMs have additional advantage related to the chiral fermions near the Weyl node, which leads to chirality-dependent photocurrent (PC).<sup>[14]</sup> Considering the essence of WSMs, in this work, a field-effect  $\text{MoTe}_2$ -based photodetector is investigated in a broadband wavelength regime (from visible 532 nm to the mid-infrared 10.6  $\mu\text{m}$ ) working in unbiased self-powered mode at room temperature. The responsivities and specific detectivities can reach 0.40  $\text{mA W}^{-1}$  and  $1.07 \times 10^8$  Jones at 532 nm and  $4.15 \times 10^{-2}$   $\text{mA W}^{-1}$  and  $9.1 \times 10^6$  Jones at 10.6  $\mu\text{m}$ , respectively. The detector exhibits fast response time in the range of 30–45  $\mu\text{s}$  over broad wavelength range. The PC generation mechanisms are investigated employing power- and temperature-dependent spatially resolved scanning photocurrent microscopy (SPCM) measurements and it is found that PTE effect plays critical role in PC generation. Furthermore, linear polarization-dependent studies indicate that the photoresponse of  $\text{MoTe}_2$  is highly anisotropic and can be used for polarization-sensitive photodetection, similar to black phosphorus (BP).<sup>[15]</sup>

The photoresponse measurements are performed on the mechanically exfoliated flakes of  $\text{T}_d$  phase  $\text{MoTe}_2$ , obtained from the bulk  $\text{MoTe}_2$ , synthesized by chemical vapor transport method.<sup>[10c]</sup> The exfoliated  $\text{MoTe}_2$  flakes are fabricated into lateral metal- $\text{MoTe}_2$ -metal devices as shown in **Figure 1a**. The  $\text{T}_d$  phase shares the same in-plane crystal structure with the 1T' phase, but has a different vertical stacking as illustrated in **Figure 1b**. As a result of the difference in stacking, 1T' phase  $\text{MoTe}_2$  belongs to centrosymmetric space group ( $P2_1/m$ ), while  $\text{T}_d$  phase  $\text{MoTe}_2$  belongs to noncentrosymmetric space group ( $Pmn2_1$ ). Experimentally, the  $\text{T}_d$  phase can be distinguished from 1T' phase by characterizing the low wavenumber Raman signal related to the shear mode at 13  $\text{cm}^{-1}$  and the out-of-plane vibration mode at 130  $\text{cm}^{-1}$ . The comparison of the characteristic Raman shift peaks of the exfoliated 22 nm-thick  $\text{MoTe}_2$  with a 1T' phase  $\text{MoTe}_2$  measured under 300 K is shown in **Figure 1c**.<sup>[16]</sup> The results indicate that the exfoliated thin  $\text{MoTe}_2$  flakes used in our measurements are  $\text{T}_d$  phase at room temperature after experiencing a cooling cycle down to 77 K and then warm up back to room temperature. Here we note the fact that 22 nm  $\text{MoTe}_2$  flake is  $\text{T}_d$  phase at room temperature is in contradiction to typical phase transition temperature below 250 K that is observed previously on bulk sample<sup>[17]</sup> and the phase transition temperature turns out to be thickness dependent as the thickness thins down below 100 nm.<sup>[18]</sup> **Figure 1d** illustrates a typical SPCM image of a  $\text{MoTe}_2$  device together with its in situ scanning reflection microscopy. The area of the sample between the two electrodes is about  $20 \times 30 \mu\text{m}$ , and the PC response is obtained from the whole device, which includes the interface of  $\text{MoTe}_2$ -metal junctions and the center of  $\text{MoTe}_2$  that are away from the metal electrodes. A positive PC is generated at the inner area of the device, while it is negative both at the edge of the device and at the  $\text{MoTe}_2$ -metal electrode junctions. In addition, we note that although the stability of few-layer  $\text{T}_d$ - $\text{MoTe}_2$  is poor in the air, the photoresponse and transport properties of the  $\text{MoTe}_2$  devices turn to be very stable under ambient conditions over many months. This is because the major layers underneath the surface are well protected from degradation for devices made from relatively thick sample.

Taking the advantage of the gapless linear dispersion in the band structure, the PC responses of the  $\text{MoTe}_2$  device should spread over a broadband wavelength range. **Figure 2a** illustrates the short-circuit PC responses at different excitation photon energies ranging from 0.12 to 2.33 eV. In this measurement, the PC responses at 0.12 and 0.31 eV are recorded using two continuous wave (CW) quantum cascade laser sources, while the responses from 0.80 to 2.33 eV are recorded by switching on/off the laser pulse (6 ps, 20 MHz) from a fiber-based white light supercontinuum source. Since the PC is measured with very different light sources at different wavelengths, it is to be noted that a direct comparison of specific detectivity for different wavelength is quite difficult because of the difference in the focused laser spot sizes and the instantaneous excitation energy. The PC responses for different excitation photon energies are measured at the maximum of positive PC as marked in SPCM of **Figure 1d** at zero bias voltage. The responsivity and detectivity for the lowest excitation energy (0.12 eV) are found to be  $4.15 \times 10^{-2}$   $\text{mA W}^{-1}$  and  $9.1 \times 10^6$  Jones, whereas for highest excitation energy (2.33 eV), they are  $0.40 \text{ mA W}^{-1}$

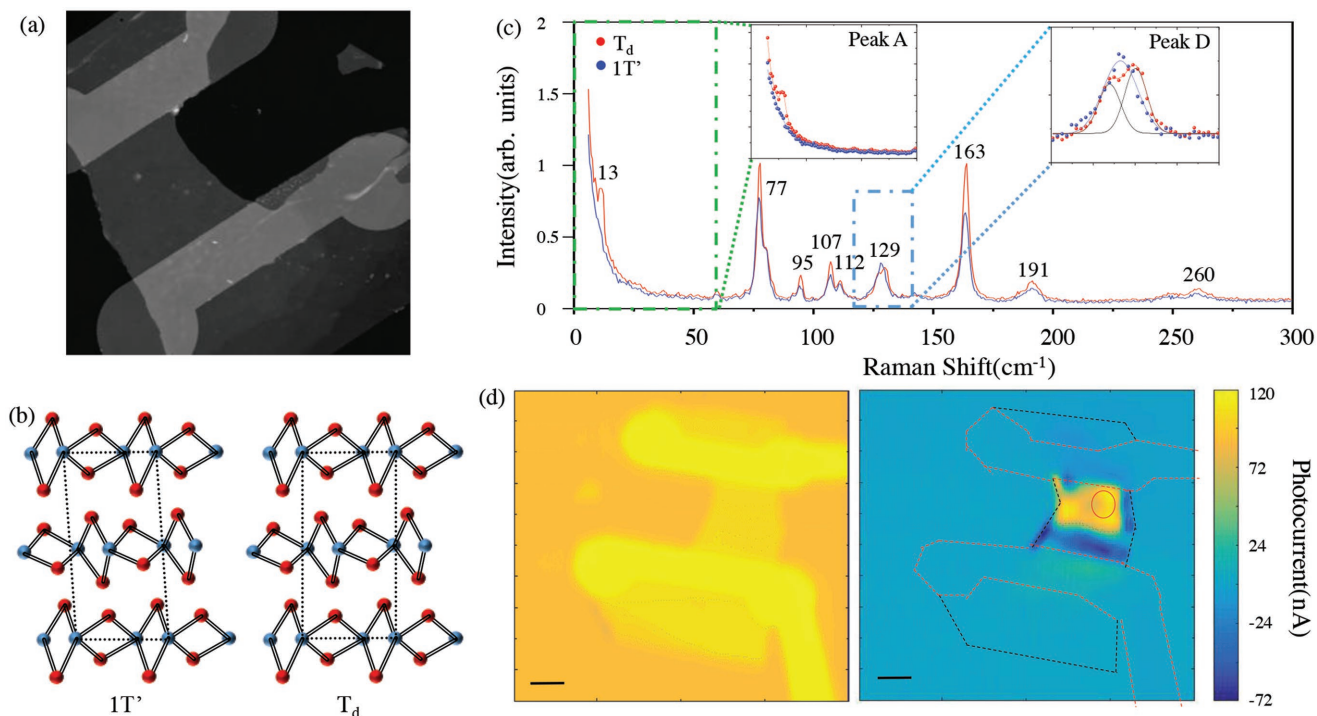


**Figure 1.** a) AFM image of the MoTe<sub>2</sub> device. b) Crystal structures of 1T' and T<sub>d</sub> phases of semimetallic MoTe<sub>2</sub>. c) Raman spectrum of 1T' and T<sub>d</sub>-MoTe<sub>2</sub> measured under 300 K. The comparison of the characteristic Raman peaks A and D are enlarged in the insets, respectively. d) SPCM images of the MoTe<sub>2</sub> device at room temperature with 633 nm excitation. Left and right panels show the reflection image and PC image, respectively. All the scale bars are 10 μm.

and  $1.07 \times 10^8$  Jones, respectively. It is worth noting that the range of response wavelength is limited by the availability of light sources for the measurements rather than the response of the device itself. As a gapless WSM, MoTe<sub>2</sub> should possess an ultrabroadband response extendable to much lower photon energy even down to THz regime, similar to graphene and Cd<sub>3</sub>As<sub>2</sub>.<sup>[19]</sup> Figure 2b shows the response time measurement through standard chopping frequency-dependent responsivity measurement at different wavelengths. The response times are 42.5, 35.8, and 31.7 μs for 532 nm, 4 μm, and 10.6 μm, respectively. These response times are comparable to commercial HgCdTe detector at mid-IR wavelength range.<sup>[3a]</sup>

In order to understand the PC generation mechanism of MoTe<sub>2</sub> photodetector, excitation power- and temperature-dependent measurements are performed on the device. The effect of excitation power and temperature on the PC response is measured by scanning a line cut crossing the maximum and minimum PC response of the device, as marked by the red lines in Figure 3b,c and Figure 4a. The power-dependent measurements are carried at 78 K by varying the power from 100 to 900 μW and the temperature dependence is measured from room temperature down to 10 K. The shape and peak position of photoresponse along the line cut remain unaffected at different excitation power (Figure 3d) and temperature (Figure 4b). Furthermore, the magnitude of PC response increases linearly with power, as shown in Figure 3e. The SPCM patterns recorded at different temperatures (illustrated in Figure 4a) also remain qualitatively same with decreasing temperature down to 10 K. However, the magnitude of PC response at the center

of the device at different temperatures does not vary monotonically, which increased as the temperature increased from 10 to 50 K and then decreased as the temperature further increased to room temperature.

The nonlocal PC generation away from the contact region and the temperature dependence of the PC amplitude imply that the PTE plays a crucial role in the PC generation. Generally, three different kinds of electron-hole separation mechanisms can account for the PC generation in the device when no external bias is applied: photovoltaic (PV) effect, photo-Dember (PD) effect, and PTE effect.<sup>[5]</sup> The PV effect separates photo-generated electron-hole pairs by built-in electric field at the interface between metal electrode and MoTe<sub>2</sub>, as metal electrode and MoTe<sub>2</sub> have different work functions. Hence, the PC generated by PV effect is highly localized along the interface between MoTe<sub>2</sub> and metal electrode, where the built-in electric field exists. In case of PD effect, the charge separation is the result of the formation of a charge dipole after photogeneration of charge carriers, owing to the different electron and hole mobility. For T<sub>d</sub>-MoTe<sub>2</sub>, though there are variations in the absolute values of carrier mobility reported in the literatures, the mobility of electron and hole of T<sub>d</sub>-MoTe<sub>2</sub> in all reports so far are very different.<sup>[20]</sup> In addition, for PD effect to happen, it is also mandatory to break the symmetry of the centrosymmetric movement of electron and hole; otherwise, the net positive and negative charge center will not separate during the movement. In this device, the symmetry breaking is provided by the metal electrode, which leads to an effective charge separation in the direction that is perpendicular to the metal electrode.<sup>[21]</sup>

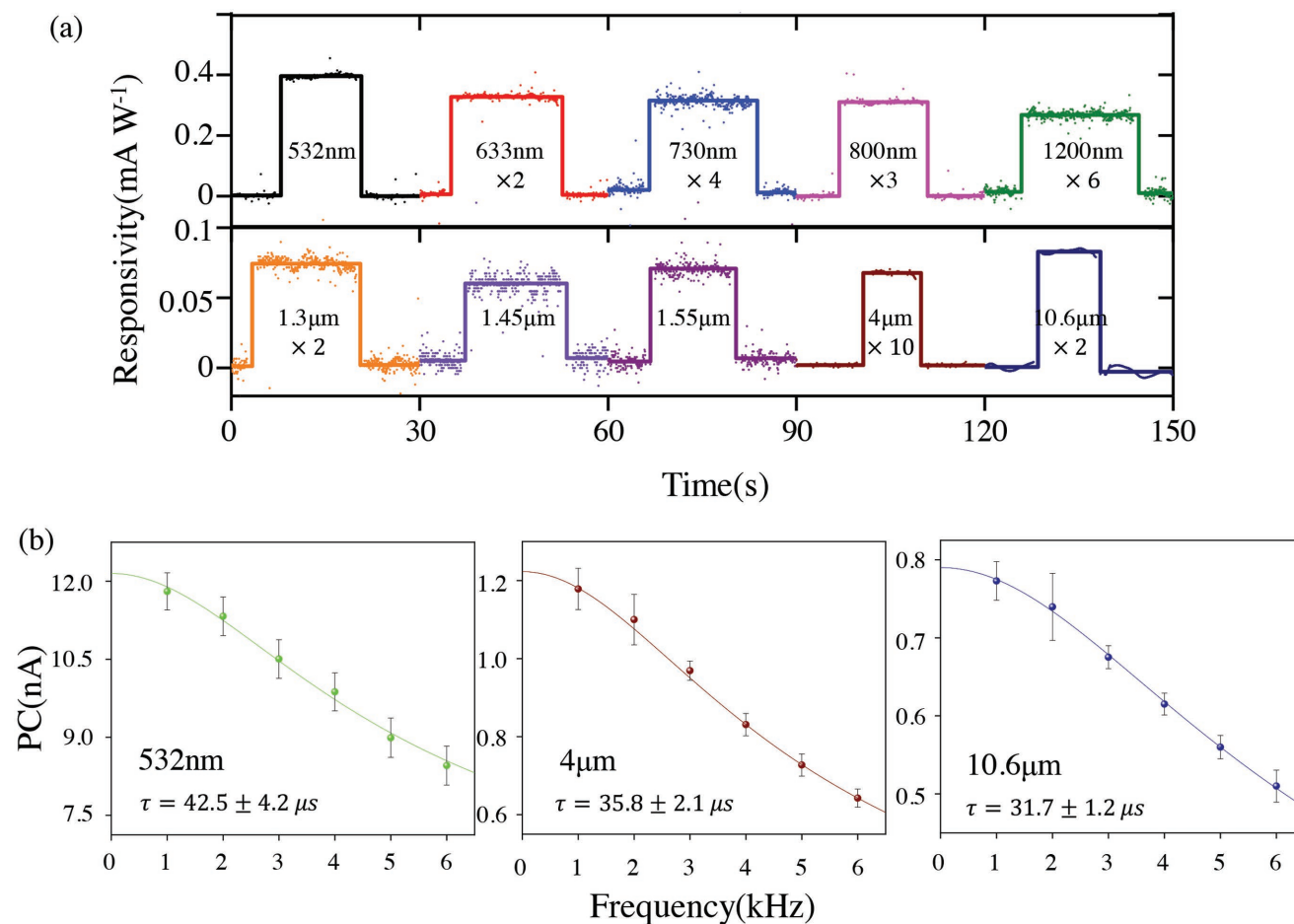


**Figure 2.** a) Photoresponse of the MoTe<sub>2</sub> device (illuminated at the position as marked by the red circle in Figure 1d) for different excitation wavelengths at 293 K. For better visualization, the magnitude of low responsivities obtained for some wavelengths is multiplied by a factor as labeled in the figure. All the scale bars are 10  $\mu\text{m}$ . b) Chopping frequency–dependent responsivity measurement with a lock-in amplifier under 532 nm, 4  $\mu\text{m}$ , and 10.6  $\mu\text{m}$  excitation, respectively. The deduced response times of different wavelengths are marked in the figure.

As a consequence, the PC generation due to PD effect is also highly localized to the interface between MoTe<sub>2</sub> and metal electrode, within the mean free path of the high mobility carriers. According to the above discussions, both PV and PD effects cannot account for the photoresponse that spreads over several micrometers away from the electrode. Therefore, PTE effect is the underlying mechanism for the generation of nonlocal photoresponse.

The PTE effect is the result of electron temperature gradient generated by photoexcitation and thermoelectric power difference. Since the SiO<sub>2</sub> substrate does not conduct heat effectively as metal and semimetallic MoTe<sub>2</sub>, gold electrode is the major heat dissipation channel of the device. After photon excitation, both the steady-state electron temperature distribution and non-uniform distribution of thermoelectric power over the MoTe<sub>2</sub> sample determine the PC generated from the PTE effect. Qualitatively, the electron temperature distribution over the MoTe<sub>2</sub> sample should strongly depend on excitation positions, device geometry, excitation power, and initial electron/lattice temperature around the excitation position. According to this, the PC generation from PTE effect does not rely on the proximity of contacts and thus can contribute to the “nonlocal” response

away from the two electrodes through the well-known Shockley–Ramo mechanism similar to graphene.<sup>[22]</sup> The magnitude of PC from the PTE response can have complicated lattice temperature dependence as observed in Figure 4b, because both the Seebeck coefficient and heat capacities depend on the temperature. On the other hand, the temperature dependence of PV and PD is both the result of temperature dependence of mobility, which monotonically increases as temperature decreases.

Finally, the linear polarization dependence of PC responses of MoTe<sub>2</sub> is studied by varying the linear polarization direction of the excitation beam at different wavelengths as illustrated in Figure 5a. Interestingly, the device shows anisotropic response similar to black phosphorus.<sup>[23]</sup> The polar plots of PC response at fixed spot of the device with different excitation polarization angles at 633 nm, 4  $\mu\text{m}$ , and 10.6  $\mu\text{m}$  are shown in Figure 5b–d, respectively. At all wavelengths, the response is anisotropic, and the ratios of anisotropy ellipse are 1.19, 1.92, and 2.72 for 638 nm, 4  $\mu\text{m}$ , and 10.6  $\mu\text{m}$ , respectively, indicating the response is more anisotropic when excited with lower photon energy. It is found that the *a*- and *b*-axes of the MoTe<sub>2</sub> thin film could be independently determined using the angle-resolved PC response measurement, with the maximum PC response along

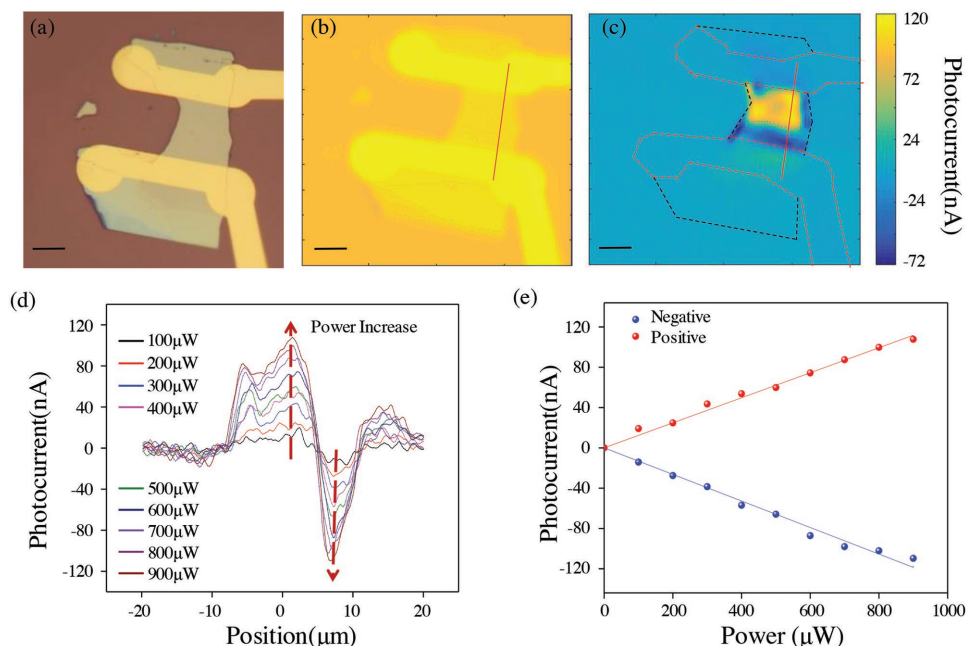


**Figure 3.** a,b) Optical microscopy and scanning reflection microscopy images of the MoTe<sub>2</sub> device, respectively. c) SPCM image of the MoTe<sub>2</sub> device with 632.8 nm excitation; the excitation power is 800 μW. d) PC response of the MoTe<sub>2</sub> device along the 40 μm line cut, marked as red line in (b) and (c), under different excitation powers varying from 100 to 900 μW at 78 K. e) The positive (red) and negative (blue) PC response as a function of excitation power. The solid lines represent the linear fit. All the scale bars are 10 μm.

the *a*-axis. A likely explanation of the anisotropy is the different effective masses and thus different absorption along the two principal axes of the MoTe<sub>2</sub> crystals.<sup>[11d,24]</sup> Similar anisotropic response is also observed on other type-II WSM candidate.<sup>[11d]</sup>

In summary, type-II WSM T<sub>d</sub>-MoTe<sub>2</sub> is experimentally verified to be an interesting high-performance photosensing material candidate. The unique physical properties of T<sub>d</sub>-MoTe<sub>2</sub> enable a self-powered broadband photodetector operating at room temperature with polarization angle sensitive response. In addition to the experimental results presented, we would like to add several important prospects regarding the photosensing potential of T<sub>d</sub>-MoTe<sub>2</sub>. First, the responsivity at longer wavelength beyond experimentally measured 10.6 μm could be much higher when the optical transition gets closer to the Weyl nodes, where the carrier mobility is much higher due to

the linear energy dispersion and the suppression of backscattering. The overall responsivity can be further enhanced using different source drain metals with interdigital contact configuration to provide opposite built-in electric field directions with MoTe<sub>2</sub>, thus avoiding the cancellation of the PC with the same source drain metal electrodes when illuminated with light spot larger than the active device channel area.<sup>[25]</sup> The PC response due to PTE mechanism could be further enhanced by fabricating suspended device over the substrate to reduce the thermal cooling through the substrate. Second, though the absence of external bias is required to avoid the dark current in semimetals, the self-powered operation could greatly facilitate wearable and portable applications, which is very attracting for wearable mid-IR sensing applications. Third, the polarization angle sensitive photoresponse of T<sub>d</sub>-MoTe<sub>2</sub> is very similar to

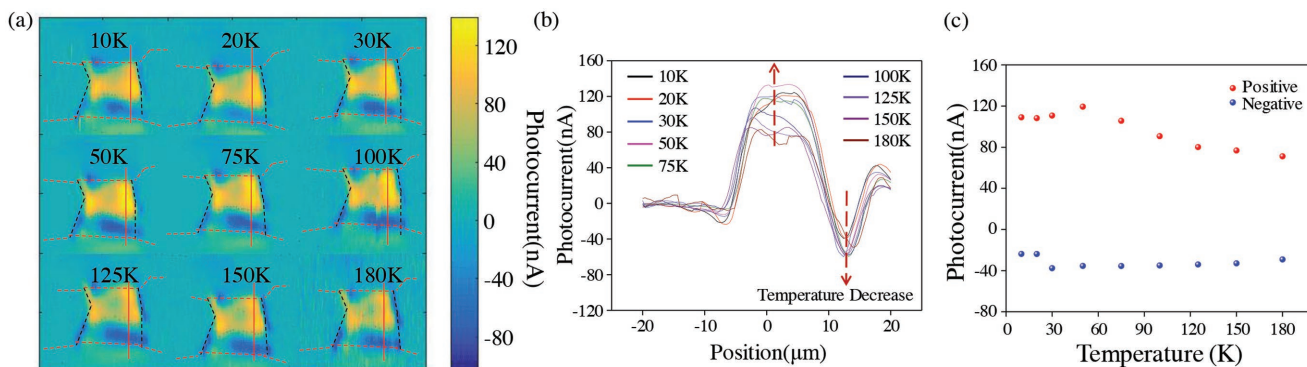


**Figure 4.** a) SPCM images of the MoTe<sub>2</sub> device at temperatures 10, 20, 30, 50, 75, 100, 125, 150, and 180 K with 632.8 nm excitation wavelength and 800 μW excitation power. b) Line cut of PC response along the red line shown in (a) at different temperatures. c) The positive (red) and negative (blue) PC response under different temperatures.

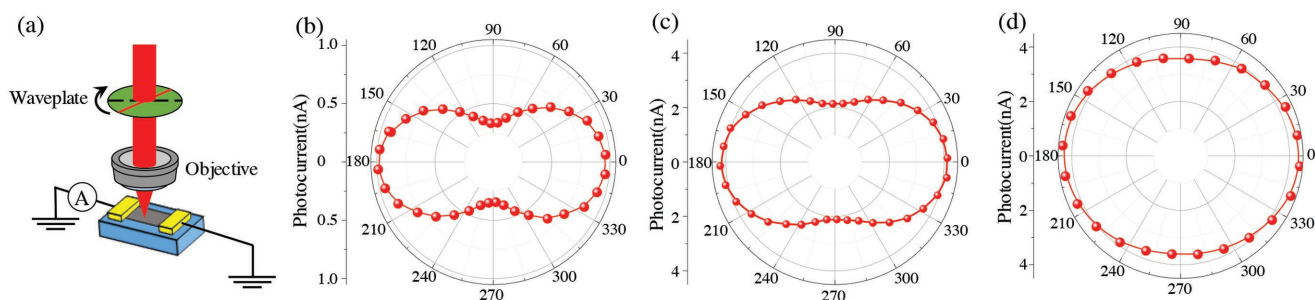


**Figure 5.** a) Schematic representation of linear polarization-dependent PC measurement setup. b–d) Anisotropic PC response for the linear polarized excitation at 10.6  $\mu\text{m}$ , 4  $\mu\text{m}$ , and 633 nm, respectively. The ratios of anisotropy ellipse are 2.72, 1.92, and 1.19, respectively.

that of BP, which is suitable for polarization-sensitive photodetection. However, in contrast to BP, where the sensing wavelength range of BP is limited by the 4  $\mu\text{m}$  bandgap,  $\text{T}_d\text{-MoTe}_2$  can be extendable beyond 4  $\mu\text{m}$ . The fortunate fact is that the response of  $\text{T}_d\text{-MoTe}_2$  is more anisotropic at longer wavelength. At last, we note that  $\text{T}_d\text{-MoTe}_2$  is a layered material, so it is ready to form van der Waals heterostructures with other layered 2D materials and conveniently incorporate advantages of other members from 2D families to further improve the performance of photosensing. From this consideration,  $\text{T}_d\text{-MoTe}_2$  is endowed with many possibilities as a 2D layered material surpassing  $\text{Cd}_3\text{As}_2$ , a 3D DSM, which is a good sensing material with excellent performance comparable to  $\text{T}_d\text{-MoTe}_2$  in terms of responsivity and broadband response.

## Experimental Section

**Sample Growth:** High-quality  $\beta\text{-MoTe}_2$  single crystals were grown by chemical vapor transport using polycrystalline  $\text{MoTe}_2$  as precursors. Briefly, polycrystalline  $\text{MoTe}_2$  was synthesized by heating the stoichiometric mixture of high-purity Mo foil (99.95%, Alfa Aesar) and Te ingot (99.99%, Alfa Aesar) at 1073 K in a vacuum-sealed silica ampule for 3 d. The as-grown  $\text{MoTe}_2$  was then recrystallized by chemical vapor transport method using the transporting agent, powder  $\text{TeCl}_4$  (99%, Aladdin), with a concentration of  $\leq 2.7 \text{ mg mL}^{-1}$ . Material transport occurred in a sealed silica ampule in a tube furnace for 3 d. After the reaction, the ampule was immediately quenched in cold water to obtain large-size  $\beta\text{-MoTe}_2$  single crystals.<sup>[10c]</sup>

**Device Fabrication:** The thin  $\text{MoTe}_2$  samples used for the studies in this letter were mechanically exfoliated from bulk  $\text{MoTe}_2$  crystal and transferred on to 300 nm  $\text{SiO}_2/\text{Si}$  substrates. Standard electron-beam lithography technique was used to pattern electrodes, two-terminals, consisting of 5 nm Cr and 50 nm Au.

**Raman Characterization:** Raman spectra acquired in a confocal backscattering geometry using an Argon laser of 514 nm for excitation. The Raman spectra were analyzed using a Horiba Jobin Yvon LabRAM HR Evolution spectrometer, equipped with 1800  $\text{gr mm}^{-1}$  gratings, a liquid nitrogen-cooled CCD detector, and Bragg Grate notch filters that allow for measurements down to low wave numbers. The temperature of the samples was controlled by a liquid-helium flow cryostat.

**Photoresponse Measurements:** Standard scanning photocurrent measurements were performed in ambient conditions using 632.8 nm CW He-Ne laser with  $\approx 1 \mu\text{m}$  spatial resolution. The laser beam was focused by a 40 $\times$  transmissive objective lens. A scanning mirror was used to scan the light beam on the sample. The reflection signal and PC were recorded simultaneously to get the reflection image and PC response. For wavelength-dependent measurements, a series of bandpass filters were used to select the desired wavelength from

a white light supercontinuum output of Fianium: WhiteLase-Micro (20 MHz, 6 ps, 450–2200 nm). Two CW quantum cascade laser sources emitting at 4 and 10.6  $\mu\text{m}$  are used for mid-infrared measurement. The mid-IR beams were focused by a 40 $\times$  reflection objective instead. For polarization-dependent PC measurements, a 5 $\times$  objective was used to focus the 632.8 nm laser beam with a spot diameter of about 20  $\mu\text{m}$  and a 40 $\times$  reflection objective was used to focus the 10.6  $\mu\text{m}$  laser beam with a spot diameter of about 25  $\mu\text{m}$ , which covered the whole sample to minimize the possible effect of sample drift during the measurements. A motorized rotation stage was used to rotate a half waveplate for the linear polarization-dependent measurement. The laser beam was modulated with a mechanical chopper (383 Hz), and the short-circuit PC signal was detected with a current pre-amplifier and a lock-in amplifier.

Response time measurements were performed in ambient conditions using CW excitation and an optical chopper with different chopping frequencies. The photocurrent response ( $R_f$ ) taken from a lock-in amplifier as a function of the different chopping frequencies ( $f$ ) was fitted with  $R_f = R_0 / \sqrt{1 + (2\pi f\tau)^2}$  to obtain the response time ( $\tau$ ).

## Acknowledgements

This project was supported by the National Basic Research Program of China (973 Grant No. 2014CB920900), National Key Research and Development Program of China (Grant No. 2016YFA0300802), the National Natural Science Foundation of China (NSFC Grant Nos. 91750109, 11674013, and 11704012), the Recruitment Program of Global Experts, the State Key Laboratory of Precision Measurement Technology and Instruments Fund for open topics and the China Postdoctoral Science Foundation (Grant No. 2017M610009).

## Conflict of Interest

The authors declare no conflict of interest.

## Keywords

anisotropy, photodetectors, Weyl semimetals

Received: December 7, 2017  
Revised: February 11, 2018  
Published online: April 17, 2018

- [1] a) D. S. Tsai, C. A. Lin, W. C. Lien, H. C. Chang, Y. L. Wang, J. H. He, *ACS Nano* **2011**, *5*, 7748; b) A. Gassenq, F. Gencarelli, J. Van Campenhout, Y. Shimura, R. Loo, G. Narcy, B. Vincent, G. Roelkens, *Opt. Express* **2012**, *20*, 27297; c) B. Y. Zhang, T. Liu,

- B. Meng, X. Li, G. Liang, X. Hu, Q. J. Wang, *Nat. Commun.* **2013**, *4*, 1811; d) S. Nanot, A. W. Cummings, C. L. Pint, A. Ikeuchi, T. Akiho, K. Sueoka, R. H. Hauge, F. Leonard, J. Kono, *Sci. Rep.* **2013**, *3*, 1335; e) C. H. Liu, Y. C. Chang, T. B. Norris, Z. H. Zhong, *Nat. Nanotechnol.* **2014**, *9*, 273.
- [2] a) A. Rogalski, *Prog. Quantum Electron.* **2003**, *27*, 59; b) Q. Wang, J. Lai, D. Sun, *Opt. Mater. Express* **2016**, *6*, 2313.
- [3] a) A. Rogalski, *Rep. Prog. Phys.* **2005**, *68*, 2267; b) Z. Sun, Z. Liu, J. Li, G. A. Tai, S. P. Lau, F. Yan, *Adv. Mater.* **2012**, *24*, 5878; c) A. Munoz, J. Melendez, M. C. Torquemada, M. T. Rodrigo, J. Cebrian, A. J. de Castro, J. Meneses, M. Ugarte, F. Lopez, G. Vergara, J. L. Hernandez, J. M. Martin, L. Adell, M. T. Montojo, *Thin Solid Films* **1998**, *317*, 425.
- [4] a) F. Xia, T. Mueller, Y. M. Lin, A. Valdes-Garcia, P. Avouris, *Nat. Nanotechnol.* **2009**, *4*, 839; b) D. Sun, G. Aivazian, A. M. Jones, J. S. Ross, W. Yao, D. Cobden, X. Xu, *Nat. Nanotechnol.* **2012**, *7*, 114; c) K. J. Tielrooij, L. Piatkowski, M. Massicotte, A. Woessner, Q. Ma, Y. Lee, K. S. Myhro, C. N. Lau, P. Jarillo-Herrero, N. F. van Hulst, F. H. Koppens, *Nat. Nanotechnol.* **2015**, *10*, 437; d) Z. Q. Li, E. A. Henriksen, Z. Jiang, Z. Hao, M. C. Martin, P. Kim, H. L. Stormer, D. N. Basov, *Nat. Phys.* **2008**, *4*, 532; e) F. Wang, Y. Zhang, C. Tian, C. Girit, A. Zettl, M. Crommie, Y. R. Shen, *Science* **2008**, *320*, 206.
- [5] Q. Wang, C. Z. Li, S. Ge, J. G. Li, W. Lu, J. Lai, X. Liu, J. Ma, D. P. Yu, Z. M. Liao, D. Sun, *Nano Lett.* **2017**, *17*, 834.
- [6] S. Chi, Z. Li, Y. Xie, Y. Zhao, Z. Wang, L. Li, H. Yu, G. Wang, H. Weng, H. Zhang, J. Wang, **2017**, *arXiv: 1705.05086*.
- [7] a) X. G. Wan, A. M. Turner, A. Vishwanath, S. Y. Savrasov, *Phys. Rev. B* **2011**, *83*, 205101; b) H. M. Weng, C. Fang, Z. Fang, B. A. Bernevig, X. Dai, *Phys. Rev. X* **2015**, *5*, 011029.
- [8] a) S. M. Huang, S. Y. Xu, I. Belopolski, C. C. Lee, G. Chang, B. Wang, N. Alidoust, G. Bian, M. Neupane, C. Zhang, S. Jia, A. Bansil, H. Lin, M. Z. Hasan, *Nat. Commun.* **2015**, *6*, 7373; b) B. Q. Lv, N. Xu, H. M. Weng, J. Z. Ma, P. Richard, X. C. Huang, L. X. Zhao, G. F. Chen, C. E. Matt, F. Bisti, V. N. Strocov, J. Mesot, Z. Fang, X. Dai, T. Qian, M. Shi, H. Ding, *Nat. Phys.* **2015**, *11*, 724; c) L. X. Yang, Z. K. Liu, Y. Sun, H. Peng, H. F. Yang, T. Zhang, B. Zhou, Y. Zhang, Y. F. Guo, M. Rahn, D. Prabhakaran, Z. Hussain, S. K. Mo, C. Felser, B. Yan, Y. L. Chen, *Nat. Phys.* **2015**, *11*, 728; d) B. Q. Lv, H. M. Weng, B. B. Fu, X. P. Wang, H. Miao, J. Ma, P. Richard, X. C. Huang, L. X. Zhao, G. F. Chen, Z. Fang, X. Dai, T. Qian, H. Ding, *Phys. Rev. X* **2015**, *5*, 031013; e) X. C. Huang, L. X. Zhao, Y. J. Long, P. P. Wang, D. Chen, Z. H. Yang, H. Liang, M. Q. Xue, H. M. Weng, Z. Fang, X. Dai, G. F. Chen, *Phys. Rev. X* **2015**, *5*, 031023; f) B. Xu, Y. M. Dai, L. X. Zhao, K. Wang, R. Yang, W. Zhang, J. Y. Liu, H. Xiao, G. F. Chen, A. J. Taylor, D. A. Yarotski, R. P. Prasankumar, X. G. Qiu, *Phys. Rev. B* **2016**, *93*, 121110.
- [9] A. A. Soluyanov, D. Gresch, Z. Wang, Q. Wu, M. Troyer, X. Dai, B. A. Bernevig, *Nature* **2015**, *527*, 495.
- [10] a) I. Belopolski, S.-Y. Xu, Y. Ishida, X. Pan, P. Yu, D. S. Sanchez, H. Zheng, M. Neupane, N. Alidoust, G. Chang, T.-R. Chang, Y. Wu, G. Bian, S.-M. Huang, C.-C. Lee, D. Mou, L. Huang, Y. Song, B. Wang, G. Wang, Y.-W. Yeh, N. Yao, J. E. Rault, P. Le Fèvre, F. Bertran, H.-T. Jeng, T. Kondo, A. Kaminski, H. Lin, Z. Liu, F. Song, S. Shin, M. Z. Hasan, *Phys. Rev. B* **2016**, *94*, 085127; b) T.-R. Chang, S.-Y. Xu, G. Chang, C.-C. Lee, S.-M. Huang, B. Wang, G. Bian, H. Zheng, D. S. Sanchez, I. Belopolski, N. Alidoust, M. Neupane, A. Bansil, H.-T. Jeng, H. Lin, M. Zahid Hasan, **2016**, *7*, 10639; c) K. Deng, G. L. Wan, P. Deng, K. N. Zhang, S. J. Ding, E. Y. Wang, M. Z. Yan, H. Q. Huang, H. Y. Zhang, Z. L. Xu, J. Denlinger, A. Fedorov, H. T. Yang, W. H. Duan, H. Yao, Y. Wu, S. S. Fan, H. J. Zhang, X. Chen, S. Y. Zhou, *Nat. Phys.* **2016**, *12*, 1105; d) L. Huang, T. M. McCormick, M. Ochi, Z. Zhao, M. T. Suzuki, R. Arita, Y. Wu, D. Mou, H. Cao, J. Yan, N. Trivedi, A. Kaminski, *Nat. Mater.* **2016**, *15*, 1155; e) K. Koepnick, D. Kasinathan, D. V. Efremov, S. Khim, S. Borisenko, B. Buchner, J. van den Brink, *Phys. Rev. B* **2016**, *93*, 201101; f) Y. Sun, S. C. Wu, M. N. Ali, C. Felser, B. H. Yan, *Phys. Rev. B* **2015**, *92*, 161107; g) A. Tamai, Q. S. Wu, I. Cucchi, F. Y. Bruno, S. Ricco, T. K. Kim, M. Hoesch, C. Barreteau, E. Giannini, C. Besnard, A. A. Soluyanov, F. Baumberger, *Phys. Rev. X* **2016**, *6*, 031021; h) Z. Wang, D. Gresch, A. A. Soluyanov, W. Xie, S. Kushwaha, X. Dai, M. Troyer, R. J. Cava, B. A. Bernevig, *Phys. Rev. Lett.* **2016**, *117*, 056805.
- [11] a) Y. Wang, E. Liu, H. Liu, Y. Pan, L. Zhang, J. Zeng, Y. Fu, M. Wang, K. Xu, Z. Huang, Z. Wang, H. Z. Lu, D. Xing, B. Wang, X. Wan, F. Miao, *Nat. Commun.* **2016**, *7*, 13142; b) S. Khim, K. Koepnick, D. V. Efremov, J. Klotz, T. Förster, J. Wosnitza, M. I. Sturza, S. Wurmehl, C. Hess, J. van den Brink, B. Büchner, *Phys. Rev. B* **2016**, *94*, 165145; c) I. Belopolski, P. Yu, D. S. Sanchez, Y. Ishida, T.-R. Chang, S. S. Zhang, S.-Y. Xu, H. Zheng, G. Chang, G. Bian, H.-T. Jeng, T. Kondo, H. Lin, Z. Liu, S. Shin, M. Z. Hasan, *Nat. Commun.* **2017**, *8*, 942; d) A. J. Frenzel, C. C. Homes, Q. D. Gibson, Y. M. Shao, K. W. Post, A. Charnukha, R. J. Cava, D. N. Basov, *Phys. Rev. B* **2017**, *95*, 245140.
- [12] a) D. Sun, Z. K. Wu, C. Divin, X. Li, C. Berger, W. A. de Heer, P. N. First, T. B. Norris, *Phys. Rev. Lett.* **2008**, *101*, 157402; b) Z. Sun, H. Chang, *ACS Nano* **2014**, *8*, 4133.
- [13] C. Shekhar, A. K. Nayak, Y. Sun, M. Schmidt, M. Nicklas, I. Leermakers, U. Zeitler, Y. Skourski, J. Wosnitza, Z. K. Liu, Y. L. Chen, W. Schnelle, H. Borrmann, Y. Grin, C. Felser, B. H. Yan, *Nat. Phys.* **2015**, *11*, 645.
- [14] C. K. Chan, N. H. Lindner, G. Refael, P. A. Lee, *Phys. Rev. B* **2017**, *95*, 041104.
- [15] H. Yuan, X. Liu, F. Afshinmanesh, W. Li, G. Xu, J. Sun, B. Lian, A. G. Curto, G. Ye, Y. Hikita, Z. Shen, S.-C. Zhang, X. Chen, M. Brongersma, H. Y. Hwang, Y. Cui, *Nat. Nanotechnol.* **2015**, *10*, 707.
- [16] K. Zhang, C. Bao, Q. Gu, X. Ren, H. Zhang, K. Deng, Y. Wu, Y. Li, J. Feng, S. Zhou, *Nat. Commun.* **2016**, *7*, 13552.
- [17] a) Y. Qi, P. Naumov, M. Ali, C. Rajamathi, W. Schnelle, O. Barkalov, M. Hanfland, S. Wu, C. Shekhar, Y. Sun, V. S. M. Schmidt, U. Schwarz, E. Pippel, P. Werner, R. Hillebrand, T. Förster, E. Kampert, S. Parkin, R. Cava, C. Felser, B. Yan, S. Medvedev, *Nat. Commun.* **2016**, *7*, 11038; b) J. Joshi, I. Stone, R. Beams, S. Krylyuk, I. Kalish, A. Davydov, P. Vora, *Appl. Phys. Lett.* **2016**, *109*, 031903; c) X. Ma, P. Guo, C. Yi, Q. Yu, A. Zhang, J. Ji, Y. Tian, F. Jin, Y. Wang, K. Liu, T. Xia, Y. Shi, Q. Zhang, *Phys. Rev. B* **2016**, *94*, 214105.
- [18] R. He, S. Zhong, H. Kim, G. Ye, Z. Ye, L. Winford, D. McHaffie, I. Rilak, F. Chen, X. Luo, Y. Sun, A. Tsun, *Phys. Rev. B* **2018**, *97*, 041410(R).
- [19] X. Cai, A. B. Sushkov, R. J. Suss, M. M. Jadidi, G. S. Jenkins, L. O. Nyakiti, R. L. Myers-Ward, S. Li, J. Yan, D. K. Gaskill, T. E. Murphy, H. D. Drew, M. S. Fuhrer, *Nat. Nanotechnol.* **2014**, *9*, 814.
- [20] a) X. Luo, F. C. Chen, J. L. Zhang, Q. L. Pei, G. T. Lin, W. J. Lu, Y. Y. Han, C. Y. Xi, W. H. Song, Y. P. Sun, *Appl. Phys. Lett.* **2016**, *109*, 102601; b) F. C. Chen, H. Y. Lv, X. Luo, W. J. Lu, Q. L. Pei, G. T. Lin, Y. Y. Han, X. B. Zhu, W. H. Song, Y. P. Sun, *Phys. Rev. B* **2016**, *94*, 235154; c) Q. Zhou, D. Rhodes, Q. R. Zhang, S. Tang, R. Schönemann, L. Balicas, *Phys. Rev. B* **2016**, *94*, 121101.
- [21] C.-H. Liu, Y.-C. Chang, S. Lee, Y. Zhang, Y. Zhang, T. B. Norris, Z. Zhong, *Nano Lett.* **2015**, *15*, 4234.
- [22] J. C. W. Song, L. S. Levitov, *Phys. Rev. B* **2014**, *90*, 075415.
- [23] a) M. Engel, M. Steiner, P. Avouris, *Nano Lett.* **2014**, *14*, 6414; b) N. Youngblood, C. Chen, S. J. Koester, M. Li, *Nat. Photonics* **2015**, *9*, 247; c) M. Buscema, D. J. Groenendijk, S. I. Blanter, G. A. Steele, H. S. van der Zant, A. Castellanos-Gomez, *Nano Lett.* **2014**, *14*, 3347.
- [24] a) D. Chen, L. X. Zhao, J. B. He, H. Liang, S. Zhang, C. H. Li, L. Shan, S. C. Wang, Z. A. Ren, C. Ren, G. F. Chen, *Phys. Rev. B* **2016**, *94*, 174411; b) M. Ezawa, *Phys. Rev. B* **2016**, *94*, 195205; c) X. Xu, Q. Song, H. Wang, P. Li, K. Zhang, Y. Wang, K. Yuan, Z. Yang, Y. Ye, L. Dai, *ACS Appl. Mater. Interfaces* **2017**, *9*, 12601.
- [25] T. Mueller, F. N. A. Xia, P. Avouris, *Nat. Photonics* **2010**, *4*, 297.